

LETTER TO THE EDITOR

Universality of coronal properties in accreting black holes across mass and accretion rate

Sudip Chakraborty¹, Ajay Ratheesh², Francesco Tombesi^{3,4,5,6,7}, Rodrigo Nemmen^{8,9}, and Srimanta Banerjee¹⁰

¹ Université Paris Saclay, Université Paris Cité, CEA, CNRS, AIM, F-91191 Gif-sur-Yvette, France.
e-mail: sudip.chakraborty@cea.fr

² INAF-IAPS, Via del Fosso del Cavaliere 100, I-00133 Rome, Italy.

³ Department of Physics, University of Rome 'Tor Vergata', via della Ricerca Scientifica 1, 00133, Rome, Italy.

⁴ INAF - Astronomical Observatory of Rome, Via Frascati 33, I-00078 Monte Porzio Catone (Rome), Italy

⁵ Department of Astronomy, University of Maryland, College Park, MD 20742, USA

⁶ NASA/Goddard Space Flight Center, Greenbelt, MD 20771, USA

⁷ INFN - Rome Tor Vergata, via della Ricerca Scientifica 1, 00133, Rome, Italy

⁸ Universidade de São Paulo, Instituto de Astronomia, Geofísica e Ciências Atmosféricas, Departamento de Astronomia, São Paulo, SP 05508-090, Brazil

⁹ Kavli Institute for Particle Astrophysics and Cosmology (KIPAC), Stanford University, Stanford, CA 94305, USA

¹⁰ Inter University Centre for Astronomy and Astrophysics, Post bag 4, Ganeshkhind, Pune, India

ABSTRACT

Aims. Through their radio loudness, lack of thermal UV emission from the accretion disk and power-law dominated spectra, Low Luminosity AGN (LLAGN) display similarity with the hard state of stellar-mass black hole X-Ray Binaries (BHBs). In this work we perform a systematic hard X-ray spectral study of a carefully selected sample of unobscured LLAGN using archival *NuSTAR* data, to understand the central engine properties in the lower accretion regime.

Methods. We analyze the *NuSTAR* spectra of a sample of 16 LLAGN. We model the continuum emission with detailed Comptonization models.

Results. We find a strong anti-correlation between the optical depth and the electron temperature of the corona, previously also observed in the brighter Seyferts. This anti-correlation is present irrespective of the shape of the corona, and the slope of this anti-correlation in the log space for LLAGN (0.68-1.06) closely matches that of the higher accretion rate Seyferts (0.55-1.11) and hard state of BHBs (~0.87). This anti-correlation may indicate a departure from a fixed disk-corona configuration in radiative balance.

Conclusions. Our result, therefore, demonstrates a possible universality in Comptonization processes of black hole X-ray sources across multiple orders of magnitude in mass and accretion rate.

Key words. accretion, accretion disks – methods: data analysis - galaxies: active – galaxies: Seyfert – X-rays: galaxies – black hole physics – radiation mechanisms: non-thermal

1. Introduction

Low-Luminosity Active Galactic Nuclei (LLAGN) are intrinsically faint sub-Eddington accreting systems, with average bolometric luminosities $L_{\text{bol}} \sim 10^{38-43} \text{ erg s}^{-1}$ and average Eddington ratio $\lambda_{\text{Edd}} = L_{\text{bol}}/L_{\text{Edd}} \sim 10^{-2} - 10^{-5}$ (Ho 2009), L_{Edd} being the Eddington luminosity, as opposed to their luminous AGN counterparts ($\lambda_{\text{Edd}} \sim 0.1 - 1$; Kollmeier et al. 2006). It is believed that the bulk of the supermassive black hole (SMBH) population in the local universe reside in the form of underfed LLAGN (Ho et al. 1995; Ho 2008), making up the major fraction of the lifetime of SMBHs (Martini 2004; Shin et al. 2010), but contributing little to their growth.

Observationally, LLAGN differ from the luminous AGN: they lack significant X-ray variability (Pellegrini et al. 2000; Ho 2008), their broadband SEDs (Spectral Energy Distributions) have no quasar-like “big blue bump” in the UV continuum (Quataert et al. 1999) (an indicator of the standard optically thick, geometrically thin accretion disk, Ho 1999, 2008; Nemmen et al. 2006), they typically have weak or non-existent, narrow Fe K α emission line (Terashima et al. 2002) along with the

occasional presence of broad double-peaked H α lines (Storchi-Bergmann et al. 2003) - all consistent with the absence of a thin accretion disk or the presence of a truncated thin accretion disk (truncated at $\geq 100GM/c^2$, Chen et al. 1989). Furthermore, all of these observational evidences hint towards the LLAGN accretion mode likely being Advection-Dominated Accretion Flows (ADAF; Narayan et al. 1998; Nemmen et al. 2014), in which the hot, geometrically thick, optically thin accretion flow has typically low radiative efficiencies ($L \ll 0.1\dot{M}c^2$) and low accretion rate ($\dot{M} \lesssim 0.01\dot{M}_{\text{Edd}}$). Relativistic jets are also thought to play an important role throughout the LLAGN broadband SED (Pian et al. 2010; Nemmen et al. 2014; Fernández-Ontiveros et al. 2023). Furthermore, LLAGNs do not follow some of the correlations established in their higher luminosity counterparts (e.g., instead of the positive Γ vs λ_{Edd} correlation in brighter AGNs (Sobolewska & Papadakis 2009), LLAGNs show an anti-correlation between the two parameters; Gu & Cao 2009; Yang et al. 2015; She et al. 2018).

The X-ray spectrum of AGN is usually dominated by a primary power-law component, attributed to a hot plasma (monikered the ‘corona’; Haardt & Maraschi 1991; Haardt et al.

1997) Compton up-scattering the optical/UV photons emitted by the underlying accretion disk into the X-ray band. A high-energy cut-off in the hard X-ray spectrum, indicative of the temperature of the corona, is one of the important signatures of this Comptonization process (Baloković et al. 2015; Brenneman et al. 2014). Additionally, reflection features, in the form of an iron line complex around ~ 6.4 keV as well as a “Compton hump” at ~ 20 – 40 keV, are sometimes present. The simplest description of Comptonizing coronae is obtained by measuring the photon power-law index and the cut-off in the hard X-ray spectrum. The former depends on the interplay between the electron temperature and the optical depth, whereas the latter is directly related to the electron temperature of the corona. While in brighter AGN, the primary source of X-ray photons is considered as the unsaturated Comptonization of thermal photons from a standard geometrically thin, optically thick accretion disk (Shakura & Sunyaev 1973), for LLAGN the contribution might also originate from the synchrotron self-Compton emission. Therefore, to compare and understand the coronal properties between the brighter AGN and the LLAGN, hard X-ray observations are of paramount importance.

While the brightest AGN have been studied extensively in the past with hard X-ray satellites, such as BeppoSAX (Dadina 2007), INTEGRAL (Molina et al. 2013) and *Swift*-BAT (Ricci et al. 2017), hard X-ray class studies of LLAGN is sparse (e.g., Diaz et al. 2023). The Nuclear Spectroscopic Telescope Array (*NuSTAR*, Harrison et al. 2013), the first focusing X-ray telescope at hard X-rays, allows us to systematically study the hard X-ray signatures of LLAGN in unprecedented details thanks to its focusing optics, broad and high-quality spectral coverage between 3 to 79 keV. Therefore, *NuSTAR* is suitable for studying the hard X-ray spectra of AGN with high sensitivity, discriminating between the primary X-ray emission and the reflected component. Alone, or with simultaneous observations with other X-ray observatories operating below 10 keV, such as XMM-Newton, Suzaku and *Swift*-XRT, it has provided strong constraints on the coronal properties of many bright AGN (Brenneman et al. 2014; Fabian et al. 2015; Matt et al. 2015; Fabian et al. 2017; Tortosa et al. 2018).

Recently, Tortosa et al. (2018) studied the coronal properties of a sample of bright Seyferts using *NuSTAR* spectra. Along with the previously reported correlations, they have found clear indications of unexplained anti-correlation between the electron temperature and the optical depth. To explore the validity of these correlations at much lower luminosities, a systematic Comptonization study of LLAGN with *NuSTAR* has to be carried out. In our present work, we aim to bridge this gap. In section 2, we discuss our sample selection. In section 3, we explore the selected sample of LLAGN with different spectral models and find the correlations between the important parameters. We present the key results in section 4. Finally, in section 5, we discuss the implications of this study.

2. Data selection

The sample considered in this work was selected predominantly from Palomar sample (Saikia et al. 2018; Nagar et al. 2005), and supplemented with sources from the BASS DR1¹ (Ricci et al. 2017), as well as the following works: Nemmen et al. (2014); Kawamuro et al. (2016); Ho (2009); Hernández-García et al. (2016); González-Martín & Vaughan (2012); Eracleous et al. (2010); Terashima et al. (2002); Ursini et al. (2015). Since the

main motive of this work is to study the properties of the central engine in these sources, we identified unobscured, Compton-thin LLAGN by imposing upper constraint of 10^{24} cm⁻² on the hydrogen equivalent column density (N_{H}) and $\sim 10^{43}$ erg/s on the bolometric luminosity. All the sources and the corresponding *NuSTAR* data used in this work are outlined in Table. D.1. Methods of reduction of *NuSTAR* data is given in Appendix A. We also impose a minimum count-rate threshold of 4×10^{-2} cts/s in the 3-79 keV energy range in both FPMA and FPMB to reach a satisfactory signal-to-noise level for spectral analysis. This produces the 16 sources, described in table D.1, constituting our sample. For details on the uniform reduction of the *NuSTAR* data, see Appendix A.

3. Spectral Analysis

The spectral fitting and statistical analysis are carried out using the XSPEC version v-12.12.0 (Arnaud 1996). To jointly fit FPMA and FPMB, a cross-normalization constant (CONSTANT model in XSPEC) is allowed to vary freely for FPMB and is assumed to be unity for FPMA. We also restrict the energy ranges of the individual datasets to 3-25, 3-50 or 3-79 keV, based on the quality of the data. All the models, as described below, include the Galactic absorption through the implementation of the TBABS model. The corresponding abundances are set as per the solar abundances in Wilms et al. (2000). The neutral hydrogen column densities (N_{H}) are fixed to values found in the literature (see table D.1) for all the described models. All parameter uncertainties are reported at the 1σ confidence level for one parameter of interest.

To get a detailed understanding of the Comptonization processes and to directly compare with previous studies of other accreting black hole systems, we require reliable estimates of the optical depth (τ) and electron temperatures (kT_e) of the coronae. To directly fit the optical depths and electron temperatures in the 3-79 keV *NuSTAR* data, we use the Comptonization model `COMP TT` (Titarchuk 1994) in XSPEC. `COMP TT` models the thermal Comptonization emission of a hot plasma cooled by soft photons with a Wien law distribution and includes special relativistic effects. This model is valid both in the case of optically thick and optically thin plasma. The Comptonized spectrum is determined completely by the plasma temperature and the so-called β parameter which is independent of geometry. We use both the available slab and sphere geometry in this work. For the former, we set the geometry switch to 0.5, and for the latter, we set it to 2. In both cases, the corresponding β values are calculated from optical depth using analytic approximations (Titarchuk 1994). We use the redshift values mentioned in table D.1 and assume the seed black-body temperature to be fixed at 10 eV (Younes et al. 2019). In the cases where excess at Fe-K energies (around 6.4 keV) are observed, we include a Gaussian emission line (GAUSS in XSPEC). Whenever the lines are found to be too narrow to be resolved by *NuSTAR*, we freeze the width of the Gaussian line (σ) to zero. The details of the best-fit continuum parameters are presented in table D.2, while emission lines are described in table D.3. The best-fit parameters and $\chi^2/\text{d.o.f.}$ values stated in table D.2 are corrected for reflection features with physically motivated models as well, as described in the next paragraph. From table D.2, it can be seen that both the geometries of `COMP TT` model result in statistically similar fits. Physical constraints over kT_e are found for 12 and 11 cases for the slab and the sphere geometries, respectively. Out of these, the values of kT_e for NGC 4258 are found to be unphysical (< 10 keV).

¹ <https://www.bass-survey.com/dr1.html>

Of the 10 LLAGN with prominent iron lines, 4 are found to have central energies of ≥ 6.4 keV, and 6 are found to have line energies ≤ 6.4 keV. Upon further investigations on the available literature of these 10 LLAGN, the iron lines in the latter 6 were found to have AGN origin, and the former 6 are found to have originated from hot diffused gas. Most early-type galaxies emit an extended hot diffuse X-ray component usually fitted with an emission model from an optically thin plasma (Fabbiano 1989). To account for this, we use an APEC component (Astrophysical Plasma Emission Code, Smith et al. (2001)) along with the compTT continuum to model instead of the Gaussian. We assume solar metallicity and fit for the plasma temperature. For the LLAGN with AGN-origin Fe-K lines, and to account for the occasional reflection hump noted in a few of these sources, we use the PEXMON model (Nandra et al. 2007) for reflection from a neutral medium. The model component is dependent on the inclination angle of the source, which we fix to 45° , and on elemental abundances which we assume to be solar. Compared to other similar models such as PEXRAV, PEXMON has the advantage of self-consistently including reflection due to atomic species such as the Fe $K\alpha$, Fe $K\beta$ and Ni $K\alpha$ (Nandra et al. 2007). The inclusion of APEC and PEXMON improves the fits in all the cases. Finally, in the case of NGC 5506, broad iron lines accompanied by a Compton hump at 30-50 keV, are observed. To test the possibility of relativistic broadening, we convolve the PEXMON model with smeared relativistic accretion disk line profiles using RELCONV (Dauser et al. 2010). Hereafter, we use the APEC/PEXMON-corrected kT_e values for studying correlations between the parameters to make them more robust.

4. Results

From figure 1, we observe an anti-correlation between τ and kT_e in our sample of LLAGN, for both the slab and spherical geometry of the corona. This anti-correlation is similar to the one found by Tortosa et al. (2018) for the more luminous AGN.

We find the Spearman's rank correlation coefficients between τ and kT_e (see Appendix B for details) for the LLAGN to be $\rho = -0.75 \pm 0.14$ for the spherical corona and $\rho = -0.81 \pm 0.11$ for the slab corona, with corresponding p -values of 0.003 and 0.002. The histogram of the ρ values for both the geometries are displayed in figure B.1. Such high negative values of ρ suggest strong anti-correlation between kT_e and τ for both the coronal geometries, although the anti-correlation is found to be stronger for the slab geometry.

In order to directly perform a regression analysis in the kT_e vs τ plane for our LLAGN sample, we implement the bivariate correlated errors and intrinsic scatter (BCES²), following the prescription of Akritas & Bershady (1996). We perform 5×10^4 trials and adopt the orthogonal least squares BCES line as our best fit. Fitting the kT_e and τ in the logarithmic space ($\log(kT_e) = a \log(\tau) + b$), we find the best-fit parameters to be:

For slab geometry: $a = -0.77 \pm 0.09$; $b = 1.62 \pm 0.01$

For spherical geometry: $a = -0.98 \pm 0.08$; $b = 2.04 \pm 0.03$

To compare these values directly with the ones for luminous AGN, we perform the same BCES-based fit on the kT_e vs τ data from Tortosa et al. (2018). For such bright AGN, we find the best-fit values to be:

For slab geometry: $a = -0.97 \pm 0.14$; $b = 1.53 \pm 0.15$

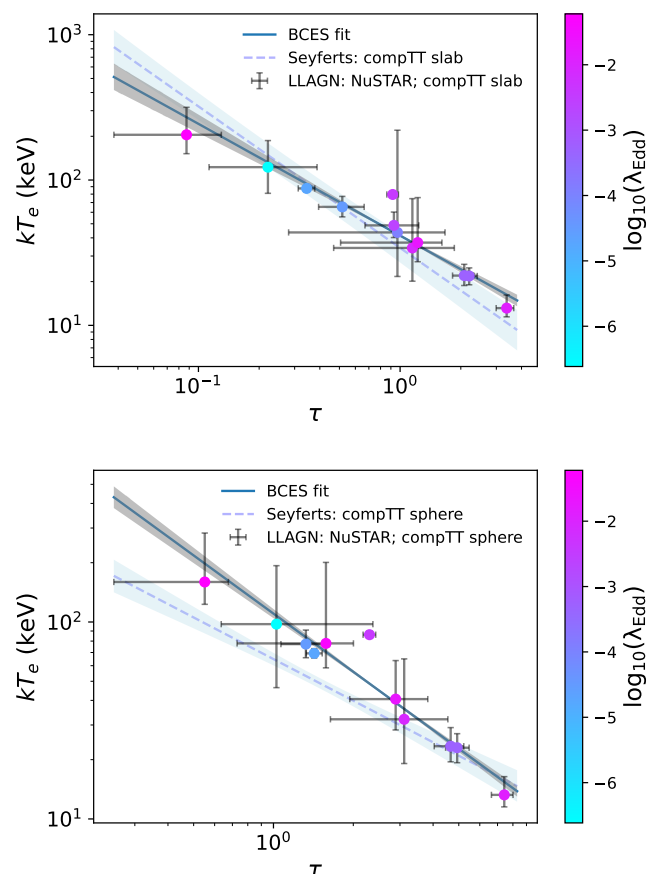


Fig. 1. The electron temperature (kT_e) vs optical depth (τ) for different geometries of the corona from the CompTT model. Top panel: slab geometry, Bottom panel: spherical geometry. In both panels, the best-fit parameters are shown along with their 1σ errorbars. The data points have been color-coded as per their Eddington ratio λ_{Edd} . The solid lines in both panels indicate the BCES best-fit lines to our LLAGN sample and the shaded grey area contains their confidence regions. For easier comparison, the best-fit line of the Seyferts (Tortosa et al. 2018) has been placed for the corresponding geometry in both panels; the BCES best-fit line is indicated with dashed blue and the corresponding confidence region in light-blue. For details about the fit, refer to section 4.

For spherical geometry: $a = -0.70 \pm 0.15$; $b = 1.81 \pm 0.05$

The kT_e vs τ plots along with the BCES best-fit lines and the corresponding confidence regions for the two geometries, are displayed in figure 1.

5. Discussions and conclusions

In this work, we probe the coronal properties of a sample of 16 carefully selected unobscured LLAGN with *NuSTAR*. We analyze the *NuSTAR* spectra using slab and sphere geometries of compTT, a model of thermal Comptonization of the seed disk photons with an assumed seed photon temperature of 10 eV. Assuming a simple parallel with Black Hole X-ray binary hard state (see the later discussions in this section), this would imply an inner edge of accretion disks at $\sim 100 - 500 R_g$. This is roughly in line with what we find for NGC 5506 (Appendix C). Although the seed photons are assumed to originate from the disk, they could also be of any other origin without considerably affecting the hard X-ray spectra, as any potential changes would primarily be observed on the lower energy side of the spectrum. We

² <https://github.com/rsnemmen/BCES>

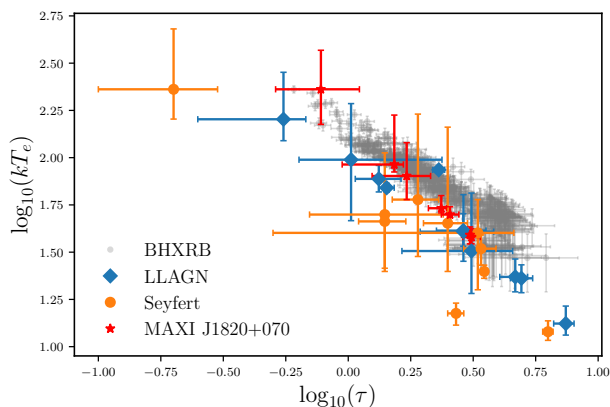


Fig. 2. The electron temperature (kT_e) vs optical depth (τ) for the spherical geometry of the corona across different class of objects: LLAGN (green), Seyferts from (Tortosa et al. 2018) (orange). For a direct comparison with the Galactic BHBs, the hard state data (with compPS model fit) from Banerjee et al. (2020) has been presented in light grey points. Furthermore, to indicate the evolution of BHBs along the presented anti-correlation, hard state data points for MAXI J1820+070 (Buisson et al. 2019) have been plotted in red. For a discussion on the implication of this universality, refer to section 5.

also investigate the iron line complex for each LLAGN, and account for the emission lines using either a diffused plasma emission using APEC, or reflection from neutral material via PEXMON. Using a uniform analysis over the entire sample, we derive robust values of kT_e and τ of the coronae. We find a similar anti-correlation between the optical depth and the electron temperatures for LLAGN, to that found in the more luminous AGN (Tortosa et al. 2018). This anti-correlation, depicted in figure 1, is found to hold true for both the slab and spherical geometry of the corona. Overall, the slab geometry is found to have more significant anti-correlation compared to the spherical geometry. The best-fit slope for LLAGN (-0.76 ± 0.09 for slab and -0.98 ± 0.08 for sphere) closely follows the slope for brighter Seyferts (-0.98 ± 0.18 for slab and 0.70 ± 0.16 for sphere).

It has been suggested for LLAGN in the ADAF regime that the scattering optical depth is related to the thickness and density of the accretion flow. This would imply that, to first order, τ is related to the mass accretion rate as $\tau = 0.03(\dot{m}/10^{-3})$ assuming a radiatively inefficient accretion flow (Narayan & Yi 1995), where \dot{m} is the accretion rate in units of the Eddington rate ($\dot{M}_{\text{Edd}} \equiv L_{\text{Edd}}/(0.1c^2)$). Taking the best-fit values found from the observations for the slab geometry, this would suggest that for LLAGNs, the electron temperature depends relatively strongly on \dot{m} as $kT_e = 599(\dot{m}/10^{-3})^{-0.77}$ keV or $kT_e = 10^{9.8}(\dot{m}/10^{-3})^{-0.77}$ K. However, no such correlation is evident between kT_e and \dot{m} or τ and \dot{m} from figure 1, although our methodology assumes a standard Comptonizing corona instead of an ADAF in the first place. For example, the Spearman’s rank coefficient between τ and λ_{Edd} is only 0.20 ± 0.16 and 0.24 ± 0.14 for spherical and slab geometry, respectively; while between kT_e and λ_{Edd} it is only -0.11 ± 0.16 and -0.18 ± 0.15 for spherical and slab geometry, respectively. This suggests that in this picture, the Comptonizing region in LLAGNs may be completely uncorrelated with the ADAF region and could instead resemble the Comptonizing coronae found in more luminous AGNs.

Remarkably, the same anti-correlation ($\rho = -0.84 \pm 0.01$) between kT_e and τ has been found for the hard state spectra of BHBs (Banerjee et al. 2020). A linear regression analysis in log-

arithmic space yields a strikingly similar slope (-0.87 ± 0.02). As the BHB data-set in Banerjee et al. (2020) uses spherical geometry of compPS model, this can be compared with the spherical geometries of our LLAGN sample or the bright AGN sample of Tortosa et al. (2018). For the BHB sample, however, the intercept is found to be slightly higher (2.17 ± 0.01). This systematic difference between BHBs and AGN would indicate that for any given τ value, the spectra of BHBs are harder (Middei et al. 2019) than their supermassive counterparts. This presence of similar anti-correlation and the remarkable similarity in Comptonization parameters across different classes of accreting black hole sources hints towards a universality of the coronal physics in all of them.

The anti-correlation between kT_e and τ indicates a departure from a fixed disk-corona configuration in radiative balance (Tortosa et al. 2018). The invalidation of a fixed disk-corona configuration can possibly occur due to a change in the coronal geometry. For example, a reduction of coronal height (in the lamppost configuration) would imply a larger Compton cooling from the disk (with an increase of τ) and, thereby, a smaller kT_e . Such a variation in the coronal geometry was earlier proposed to explain the evolution of spectral and timing features of the BHB MAXI J1820+070 in the hard state (Kara et al. 2019; Buisson et al. 2019). And, as can be seen from the red points in figure 2, MAXI J1820+070 also occupies a similar parameter space along the $kT_e - \tau$ anti-correlation line as it evolves from its hard state and its corona contracts. On the other hand, the violation of radiative balance due to a change in the disk fraction (i.e., the fraction of intrinsic disk emission to the total flux) for a fixed disk-corona system can also expound this anti-correlation (Tortosa et al. 2018). The disk fraction can alter if the inner edge of the accretion disk evolves as the supply of the soft seed disk photons to the corona depend upon this. Thus, as the disk recedes, the disk fraction falls, and the average number of scattering of thermal seed photons with coronal electrons decreases (i.e., optical depth drops). This leads to a decrease in Compton cooling and, thereby, an increase in kT_e . Hence for a highly truncated disk, τ is expected to be lower and kT_e to be higher. In our work, we find, in all three iterations of our blurred reflection model RELCONV@PEXMON implementation that the R_{in} for NGC 5506 is significantly large, indicating a highly truncated disk (see Appendix C). While the disk truncation radii for other LLAGN are not confirmed, there are indications that LLAGN, as a population, might occupy the hard state branch (usually associated with large disk truncation, e.g. Done et al. 2007) in the ‘q’-diagram (Fernández-Ontiveros et al. 2023).

References

- Akritas, M. G. & Bershad, M. A. 1996, *ApJ*, 470, 706
- Ananna, T. T., Urry, C. M., Ricci, C., et al. 2022a, *ApJ*, 939, L13
- Ananna, T. T., Weigel, A. K., Trakhtenbrot, B., et al. 2022b, *ApJS*, 261, 9
- Arnaud, K. A. 1996, *Astronomical Society of the Pacific Conference Series*, Vol. 101, *XSPEC: The First Ten Years*, ed. G. H. Jacoby & J. Barnes, 17
- Baloković, M., Matt, G., Harrison, F. A., et al. 2015, *ApJ*, 800, 62
- Banerjee, S., Gilfanov, M., Bhattacharyya, S., & Sunyaev, R. 2020, *MNRAS*, 498, 5353
- Brenneman, L. W., Madejski, G., Fuerst, F., et al. 2014, *ApJ*, 788, 61
- Buisson, D. J. K., Fabian, A. C., Barret, D., et al. 2019, *MNRAS*, 490, 1350
- Chen, K., Halpern, J. P., & Filippenko, A. V. 1989, *ApJ*, 339, 742
- Dadina, M. 2007, *A&A*, 461, 1209
- Dauser, T., Wilms, J., Reynolds, C. S., & Brenneman, L. W. 2010, *MNRAS*, 409, 1534
- Diaz, Y., Hernández-García, L., Arévalo, P., et al. 2023, *A&A*, 669, A114
- Done, C., Gierliński, M., & Kubota, A. 2007, *A&A Rev.*, 15, 1
- Eracleous, M., Hwang, J. A., & Flohic, H. M. L. G. 2010, *ApJ*, 711, 796
- Fabbiano, G. 1989, *ARA&A*, 27, 87
- Fabian, A. C., Lohfink, A., Belmont, R., Malzac, J., & Coppi, P. 2017, *MNRAS*, 467, 2566
- Fabian, A. C., Lohfink, A., Kara, E., et al. 2015, *MNRAS*, 451, 4375
- Fernández-Ontiveros, J. A., López-López, X., & Prieto, A. 2023, *A&A*, 670, A22
- González-Martín, O. & Vaughan, S. 2012, *A&A*, 544, A80
- Gu, M. & Cao, X. 2009, *MNRAS*, 399, 349
- Haardt, F. & Maraschi, L. 1991, *ApJ*, 380, L51
- Haardt, F., Maraschi, L., & Ghisellini, G. 1997, *ApJ*, 476, 620
- Harrison, F. A., Craig, W. W., Christensen, F. E., et al. 2013, *ApJ*, 770, 103
- Hernández-García, L., Masegosa, J., González-Martín, O., Márquez, I., & Perea, J. 2016, *ApJ*, 824, 7
- Ho, L. C. 1999, *ApJ*, 516, 672
- Ho, L. C. 2008, *ARA&A*, 46, 475
- Ho, L. C. 2009, *ApJ*, 699, 626
- Ho, L. C., Filippenko, A. V., & Sargent, W. L. 1995, *ApJS*, 98, 477
- Jana, A., Chatterjee, A., Chang, H.-K., et al. 2023, *MNRAS*[arXiv:2307.07966]
- Joye, W. A. & Mandel, E. 2003, in *Astronomical Society of the Pacific Conference Series*, Vol. 295, *Astronomical Data Analysis Software and Systems XII*, ed. H. E. Payne, R. I. Jedrzejewski, & R. N. Hook, 489
- Kara, E., Steiner, J. F., Fabian, A. C., et al. 2019, *Nature*, 565, 198
- Kawamuro, T., Ueda, Y., Tazaki, F., Terashima, Y., & Mushotzky, R. 2016, arXiv e-prints, arXiv:1604.07915
- Kollmeier, J. A., Onken, C. A., Kochanek, C. S., et al. 2006, *ApJ*, 648, 128
- Marinucci, A., Bianchi, S., Braitto, V., et al. 2018, *MNRAS*, 478, 5638
- Martini, P. 2004, in *Coevolution of Black Holes and Galaxies*, ed. L. C. Ho, 169
- Masini, A., Wijesekera, J. V., Celotti, A., & Boorman, P. G. 2022, *A&A*, 663, A87
- Matt, G., Baloković, M., Marinucci, A., et al. 2015, *MNRAS*, 447, 3029
- Mehdipour, M., Kriss, G. A., Kaastra, J. S., et al. 2021, *A&A*, 652, A150
- Middei, R., Bianchi, S., Marinucci, A., et al. 2019, *A&A*, 630, A131
- Middei, R., Marinucci, A., Braitto, V., et al. 2022, *MNRAS*, 514, 2974
- Molina, M., Bassani, L., Malizia, A., et al. 2013, *MNRAS*, 433, 1687
- Nagar, N. M., Falcke, H., & Wilson, A. S. 2005, *A&A*, 435, 521
- Nandra, K., O'Neill, P. M., George, I. M., & Reeves, J. N. 2007, *MNRAS*, 382, 194
- Narayan, R., Mahadevan, R., & Quataert, E. 1998, in *Theory of Black Hole Accretion Disks*, ed. M. A. Abramowicz, G. Björnsson, & J. E. Pringle, 148–182
- Narayan, R. & Yi, I. 1995, *ApJ*, 452, 710
- Nasa High Energy Astrophysics Science Archive Research Center (Heasarc). 2014, *HEASoft: Unified Release of FTOOLS and XANADU*
- Nemmen, R. S., Storchi-Bergmann, T., & Eracleous, M. 2014, *MNRAS*, 438, 2804
- Nemmen, R. S., Storchi-Bergmann, T., Yuan, F., et al. 2006, *ApJ*, 643, 652
- Osorio-Clavijo, N., González-Martín, O., Papadakis, I. E., Masegosa, J., & Hernández-García, L. 2020, *MNRAS*, 491, 29
- Pal, I., Stalin, C. S., Mallick, L., & Rani, P. 2022, *A&A*, 662, A78
- Pellegrini, S., Cappi, M., Bassani, L., della Ceca, R., & Palumbo, G. G. C. 2000, *A&A*, 360, 878
- Pian, E., Romano, P., Maoz, D., et al. 2010, *MNRAS*, 401, 677
- Prieto, M. A., Fernández-Ontiveros, J. A., Markoff, S., Espada, D., & González-Martín, O. 2016, *Monthly Notices of the Royal Astronomical Society*, 457, 3801
- Quataert, E., Di Matteo, T., Narayan, R., & Ho, L. C. 1999, *ApJ*, 525, L89
- Rani, P., Stalin, C. S., & Rakshit, S. 2017, *MNRAS*, 466, 3309
- Ricci, C., Trakhtenbrot, B., Koss, M. J., et al. 2017, *ApJS*, 233, 17
- Saikia, P., Körding, E., Coppejans, D. L., et al. 2018, *A&A*, 616, A152
- Shakura, N. I. & Sunyaev, R. A. 1973, *A&A*, 500, 33
- She, R., Ho, L. C., Feng, H., & Cui, C. 2018, *ApJ*, 859, 152
- Shin, M.-S., Ostriker, J. P., & Ciotti, L. 2010, *ApJ*, 711, 268
- Smith, R. K., Brickhouse, N. S., Liedahl, D. A., & Raymond, J. C. 2001, *ApJ*, 556, L91
- Sobolewska, M. A. & Papadakis, I. E. 2009, *MNRAS*, 399, 1597
- Storchi-Bergmann, T., Nemmen da Silva, R., Eracleous, M., et al. 2003, *ApJ*, 598, 956
- Terashima, Y., Iyomoto, N., Ho, L. C., & Ptak, A. F. 2002, *ApJS*, 139, 1
- Titarchuk, L. 1994, *ApJ*, 434, 570
- Tortosa, A., Bianchi, S., Marinucci, A., Matt, G., & Petrucci, P. O. 2018, *A&A*, 614, A37
- Ursini, F., Marinucci, A., Matt, G., et al. 2015, *MNRAS*, 452, 3266
- Wilms, J., Allen, A., & McCray, R. 2000, *ApJ*, 542, 914
- Wong, K.-W., Nemmen, R. S., Irwin, J. A., & Lin, D. 2017, *The Astrophysical Journal*, 849, L17
- Yang, Q.-X., Xie, F.-G., Yuan, F., et al. 2015, *MNRAS*, 447, 1692
- Younes, G., Ptak, A., Ho, L. C., et al. 2019, *ApJ*, 870, 73
- Young, A. J., McHardy, I., Emmanoulopoulos, D., & Connolly, S. 2018, *Monthly Notices of the Royal Astronomical Society*, 476, 5698–5703

Acknowledgements. We thank the anonymous reviewer for the constructive comments in improving this manuscript. This work made use of data from the NuSTAR mission, a project led by the California Institute of Technology, managed by the Jet Propulsion Laboratory, and funded by the National Aeronautics and Space Administration. We thank the NuSTAR Operations, Software and Calibration teams for their support with the execution and analysis of these observations. This research has also made use of the NuSTAR Data Analysis Software (NuSTARDAS), jointly developed by the ASI Science Data Center (ASDC, Italy) and the California Institute of Technology (USA). This project has received funding from the European Union's Horizon 2020 research and innovation programme under grant agreement n°101004168, the XMM2ATHENA project. The authors thank Prof. A. R. Rao and Prof. Sudip Bhattacharyya for their constructive suggestions and comments for improving this work, and Dr. Tonima Tasnim Ananna for the BASS DR2 estimates. RN acknowledges support by FAPESP (Fundação de Amparo à Pesquisa do Estado de São Paulo) under grants 2017/01461-2 and 2022/10460-8. We thank the anonymous referee for the constructive comments.

Appendix A: Data reduction

The *NuSTAR* data used in this work are reduced using v2.1.1 of the NuSTARDAS pipeline using the *NuSTAR* CALDB v20211020. The *nupipeline* tool was used to generate cleaned level2 event files. We used DS9 (Joye & Mandel 2003), to select the source and background region. The source region was selected manually to include the maximum source contribution and the background was selected away from the source to avoid contamination, both using $1'$ circular regions. The *nuproducts* tool was then used to extract the background subtracted source spectrum. For non-variable sources with multiple data sets, we did a combined fit by combining spectra from those observations using the *addspec* (version 1.4.0) tool of the FTOOLS (Nasa High Energy Astrophysics Science Archive Research Center (Heasarc) 2014). Before combining the spectra, we checked the source variabilities by probing the consistency between the fluxes and the photon indices for CUTOFFPL model fits of the spectra of different epochs. All the spectra were then binned using *grppha* tool of the FTOOLS to obtain at least 25 counts per bin, in order to use χ^2 -statistics.

Appendix B: Distribution of Spearman's rank correlation coefficient

To check the goodness of our anti-correlation in the presence of error bars in both τ and kT_e , we perform a Monte Carlo calculation by randomly generating simulated data points for each of the sources by using the best-fit parameter and the covariance matrix, repeating the procedure 2×10^4 times. We then calculate Spearman's rank correlation coefficient for each of the trials and note the mean and standard deviation of the resulting distribution. We calculate the p -values by calculating the number of times $\rho_{\text{sim}} \geq \rho_{\text{obs}}$ (where ρ_{sim} and ρ_{obs} are the Spearman's rank coefficient derived from the simulated in consideration and the corresponding value for the actual coefficient calculated from the data points, respectively), and dividing it by the total number of simulations. The distribution of ρ_{sim} for the slab and spherical geometry is portrayed in figure B.1 and the relevant values are stated and discussed in section 4.

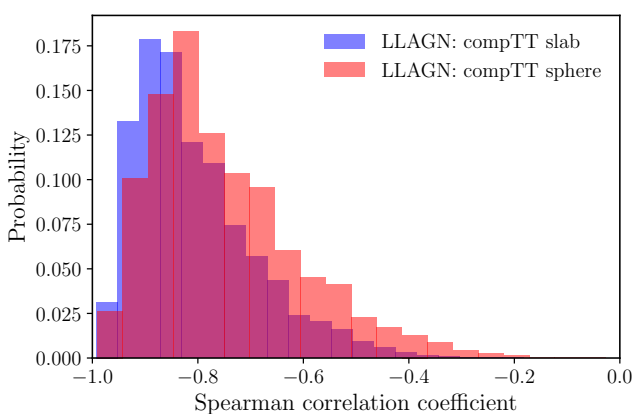


Fig. B.1. The histograms of the Spearman rank correlation coefficients (ρ) from the simulated data for the slab (blue) and spherical (red) geometries of the corona in LLAGN. While the histogram of slab geometry shows a more prominent peak at a higher ρ value than the spherical geometry, high negative mean ρ for both the geometries indicate moderate to significant anti-correlation between kT_e and τ present in both. For details about the histograms, refer to section 4.

Appendix C: Further details about specific sources: NGC 5506

For NGC 5506, $\text{COMP}\text{TT}+(\text{RELCONV}\otimes\text{PEXMON})$ resulted in a much better and more consistent fit than $\text{COMP}\text{TT}+\text{PEXMON}$. While the simple PEXMON implementation resulted in a $\chi^2/\text{d.o.f.}$ of 2057/1827, assuming the inclination to be fixed at 45° and freezing the spin parameter a to its maximum allowed value of 0.998, the $\text{RELCONV}\otimes\text{PEXMON}$ implementation gives a much better fit with a $\chi^2/\text{d.o.f.}$ of 1989/1826. The best-fit kT_e is found to be > 36.1 keV and the inner edge of accretion disk $R_{\text{in}} > 303 R_g$ (where R_g is the gravitational radius of the central black hole). Changing the inclination to 30° results in an even better fit, with a $\chi^2/\text{d.o.f.}$ of 1956/1826, the best-fit $kT_e = 78^{+131}_{-27}$ keV and $R_{\text{in}} = 126^{+26}_{-23} R_g$. Finally, letting the inclination vary freely, results in the best fit of the three cases, with a $\chi^2/\text{d.o.f.}$ of 1937/1825. This best-fit result is the one presented in table D.2 and used for the correlation study. The corresponding inclination and R_{in} are found to be $18.3^{+1.5}_{-1.3}$ degrees and $58^{+10}_{-8} R_g$, respectively.

Appendix D: Additional tables

Name	Obs ID	Date (yyyy-mm-dd)	Exposure (ks)	<i>NuSTAR</i> ref.	Spectral type	log(Mass) log(M_{\odot})	z	N_{H} ($\times 10^{22} \text{cm}^{-2}$)	log(λ_{Edd})
M81 (NGC 3031)	60101049002	2015-05-18	209	Young et al. (2018)	S1.5/L1.5	7.9	0.001	1.86	-6.62 ^a
M87 (NGC 4486)	60201016002	2017-02-15	50.0	Wong et al. (2017)	L2	9.5	0.004	0.40	-5.44 ^d
	60466002002	2018-04-24	21.1	This work					
	90202052002	2017-04-11	24.4	Wong et al. (2017)					
	90202052004	2017-04-14	22.5	Wong et al. (2017)					
NGC 1052	60061027002	2013-02-14	15.5	Rani et al. (2017)	L1.9	8.7	0.005	12.78	-3.94 ^b
	60201056002	2017-01-17	59.7	Osorio-Clavijo et al. (2020)					
	90701624002	2021-07-17	20.5	This work					
NGC 2655	60160341002	2016-11-02	0.51	Diaz et al. (2023)	S2	8.2	0.005	4.27	-3.87 ^b
	60160341004	2016-11-10	16.0	This work					
NGC 2992*	60160371002	2015-12-02	20.8	Marinucci et al. (2018)	S1.9/L1.5	8.3	0.00771	0.78	-3.30 ^b
	90501623002	2019-05-10	57.4	Middei et al. (2022)					
NGC 3227	60202002004	2016-11-25	42.0	Pal et al. (2022)	L1.9	6.7	0.004	0.09	-1.70 ^c
	60202002006	2016-11-29	39.7	Pal et al. (2022)					
	60202002008	2016-12-01	41.7	Pal et al. (2022)					
	60202002010	2016-12-05	40.9	Pal et al. (2022)					
	60202002012	2016-12-09	39.3	Pal et al. (2022)					
	60202002014	2017-01-21	47.6	Pal et al. (2022)					
NGC 3718	60301031002	2017-10-24	24.5	Diaz et al. (2023)	L1.9	8.1	0.003	0.14	-4.49 ^b
	60301031004	2017-10-27	90.4	Diaz et al. (2023)					
	60301031006	2017-10-30	57.4	Diaz et al. (2023)					
	60301031008	2017-11-03	57.0	Diaz et al. (2023)					
NGC 3998	60201050002	2016-10-25	104	Younes et al. (2019)	L1.9	8.9	0.003	0.03	-4.47 ^b
NGC 4258	60101046002	2015-11-16	54.8	Masini et al. (2022)	S1.9	7.6	0.002	8.0	-4.28 ^b
	60101046004	2016-01-10	103.6	Masini et al. (2022)					
NGC 4395	60061322002	2013-05-10	19.2	Rani et al. (2017)	S1.8	5.4	0.001	0.04	-1.90 ^a
NGC 4579	60201051002	2016-12-06	117	Younes et al. (2019)	S1.9/L1.9	8.1	0.004	0.03	-3.564 ^b
	60201056002	2017-01-17	59.7	Osorio-Clavijo et al. (2020)					
NGC 5033	60601023002	2020-12-08	103.5	Diaz et al. (2023)	S1.9	7.7	0.002	0.01	-4.00 ^b
	60601023004	2020-12-12	53.3	Diaz et al. (2023)					
NGC 5273	60061350002	2014-07-14	21.1	Rani et al. (2017)	S1.5	6.7	0.003	0.07	-2.43 ^a
	90801618002	2022-07-03	18.0	This work					
NGC 5290	60160554002	2021-07-28	18.9	Jana et al. (2023)	S2	7.8	0.009	0.91	-2.64 ^a
NGC 5506	60061323002	2014-04-01	57.0	Matt et al. (2015)	S1.9	6.0	0.006	0.31	-1.22 ^a
	60501015002	2019-12-28	61.4	This work					
	60501015004	2020-02-09	47.5	This work					
NGC 7213	60001031002	2014-10-05	109	Ursini et al. (2015)	S1.5	7.1	0.005	0.02	-2.08 ^a

Table D.1. The key properties of all the sources in our LLAGN sample and the details of its corresponding *NuSTAR* observation used in this work. For the source with *, the different observations were analyzed separately. The spectral types are abbreviated as S: Seyfert, L: LINER. z , N_{H} and λ_{Edd} denote redshift, absorbing column density and Eddington ratio, respectively. ^a:[Ananna et al. \(2022a,b\)](#), ^b:[Jana et al. \(2023\)](#), ^c:[Mehdipour et al. \(2021\)](#), ^d:[Prieto et al. \(2016\)](#)

Table D.2. Best-fit parameters of compTT models for both slab and spherical geometries in our sample of LLAGN. The corresponding errorbars are stated at 1σ levels. Here kT_e is the electron temperature of the corona and τ is its optical depth. For all the applicable LLAGN, the best-fit model includes, in addition to compTT, suitable APEC and PEXMON models. See section 3 for a detailed discussion.

LLAGN name	Sphere			Slab			3-30 keV Flux ($\times 10^{-11}$ ergs cm $^{-2}$ s $^{-1}$)
	kT_e (keV)	τ	χ^2 /d.o.f	kT_e (keV)	τ	χ^2 /d.o.f	
M81	$97.5^{+95.7}_{-51.1}$	$1.03^{+1.35}_{-0.39}$	1277/1232	$122.6^{+64.2}_{-41.6}$	$0.22^{+0.17}_{-0.11}$	1277/1232	3.40
M87	$144.3^{+3.6}_{-40.5}$	< 0.02	433.64/292	$83.2^{+1.5}_{-17.4}$	< 0.02	435.78/292	0.87
NGC1052	> 218.9	$0.27^{+0.43}_{-0.01}$	980/842	$19.2^{+6.1}_{-2.7}$	$2.33^{+0.27}_{-0.22}$	982/842	1.55
NGC 2655	$62.5^{+43.9}_{-24.2}$	$0.79^{+0.68}_{-0.46}$	65.41/50	$49.1^{+50.3}_{-16.5}$	$0.32^{+0.27}_{-0.24}$	65.58/50	0.65
NGC 2992	$23.4^{+5.7}_{-3.9}$	$4.66^{+0.56}_{-0.62}$	871.60/940	$22.0^{+4.3}_{-3.2}$	$2.08^{+0.24}_{-0.26}$	872.85/940	12.07
	$23.0^{+4.1}_{-3.7}$	$4.93^{+0.54}_{-0.47}$	1457.46/1467	$21.9^{+3.0}_{-2.8}$	$2.2^{+0.21}_{-0.19}$	1458.21/1467	17.31
NGC 3227	$40.6^{+23.1}_{-12.3}$	$2.89^{+0.93}_{-0.95}$	1901/1674	$37.1^{+38.6}_{-9.7}$	$1.22^{+0.39}_{-0.72}$	1900/1674	7.56
NGC 3718	$77.2^{+13.8}_{-11.4}$	$1.33^{+0.3}_{-0.26}$	209.03/199	$65.3^{+11.8}_{-9.6}$	$0.52^{+0.15}_{-0.12}$	209.14/199	0.22
NGC 3998	$69.3^{+3.9}_{-3.7}$	$1.42^{+0.1}_{-0.1}$	584.01/613	$87.6^{+5.0}_{-4.7}$	$0.34^{+0.03}_{-0.03}$	584.01/613	1.20
NGC 4258	$8.1^{+1.4}_{-0.9}$	$7.93^{+0.58}_{-0.72}$	607/567	$8.0^{+1.5}_{-0.8}$	$3.63^{+0.27}_{-0.36}$	607/567	0.54
NGC 4395	$137.4^{+198.9}_{-56.8}$	$2.38^{+1.14}_{-1.23}$	356.63/317	$130.8^{+152.9}_{-52.3}$	$0.92^{+0.54}_{-0.5}$	355.96/317	2.07
NGC 4579	> 84.4	$0.12^{+1.08}_{-0.0}$	652/668	> 105.9	$0.02^{+0.26}_{-0.0}$	652/668	1.20
NGC 5033	$36.1^{+198.7}_{-19.1}$	$3.33^{+2.16}_{-2.76}$	935.25/842	$26.2^{+254.7}_{-9.3}$	$1.75^{+0.66}_{-1.39}$	935.28/842	1.44
NGC 5273	$86.2^{+3.5}_{-3.3}$	$2.3^{+0.13}_{-0.12}$	752.19/721	$79.5^{+3.1}_{-3.0}$	$0.92^{+0.06}_{-0.06}$	752.78/721	3.77
NGC 5290	$41.1^{+9.4}_{-7.1}$	$2.89^{+0.67}_{-0.63}$	187/177	$48.8^{+11.5}_{-8.6}$	$0.93^{+0.31}_{-0.26}$	187/177	1.08
NGC 5506	$159.7^{+123.3}_{-36.7}$	$0.55^{+0.13}_{-0.3}$	1937.51/1825	$204.8^{+111.7}_{-53.0}$	$0.09^{+0.04}_{-0.05}$	1937.34/1825	12.37
NGC 7213	$32.1^{+32.9}_{-13.0}$	$3.11^{+1.44}_{-1.47}$	914/876	$34.1^{+40.4}_{-14.0}$	$1.15^{+0.71}_{-0.68}$	914/869	2.64

Table D.3. Best-fit parameters of the modeled reflection features in the subset of our sample of LLAGN with observed iron emission lines and/or Compton hump. For a detailed discussion, refer to section 3.

LLAGN name	Gauss		APEC	PEXMON
	Energy (keV)	Width (keV)	Energy (keV)	Refl frac
M81	$6.61^{+0.04}_{-0.04}$	$0.15^{+0.05}_{-0.05}$	$1.5^{+0.06}_{-0.05}$...
M87	$6.58^{+0.01}_{-0.03}$	0.0^f	$1.39^{+0.03}_{-0.05}$...
NGC 1052	$6.3^{+0.05}_{-0.06}$	$0.16^{+0.11}_{-0.11}$...	-0.36
NGC 2992	6.4^f	$0.38^{+0.1}_{-0.08}$...	-0.67
	6.4^f	$0.34^{+0.03}_{-0.03}$...	-0.7
NGC 3227	$6.28^{+0.02}_{-0.02}$	$0.2^{+0.04}_{-0.04}$...	-0.14
NGC 4579	$6.49^{+0.04}_{-0.04}$	$0.35^{+0.05}_{-0.04}$
NGC 5033	6.4^f	0.0^f	...	-0.86
NGC 5273	6.4^f	$0.37^{+0.08}_{-0.07}$...	-0.72
NGC 5506	$6.3^{+0.01}_{-0.01}$	$0.23^{+0.01}_{-0.02}$...	-1.0
NGC 7213	$6.53^{+0.04}_{-0.04}$	$0.33^{+0.05}_{-0.04}$	7.57	...